Journal of Materials Chemistry A

COMMUNICATION

View Article Online
View Journal

Cite this: DOI: 10.1039/c5ta09370h

Received 19th November 2015
Accepted 12th January 2016

DOI: 10.1039/c5ta09370h

www.rsc.org/MaterialsA

Alkali-modified non-precious metal 3D-$NiCo_2O_4$ nanosheets for efficient formaldehyde oxidation at low temperature†

Yongchao Huang, Wenjie Fan, Bei Long, Haibo Li, Weitao Qiu, Fengyi Zhao, Yexiang Tong* and Hongbing Ji*

Cost-effective catalysts for volatile organic compound (VOC) oxidation are critical to energy conversion and environmental protection. Herein, we developed new, low-cost and high-performance alkali-promoted 3D-$NiCo_2O_4$ nanosheet catalysts for HCHO oxidation at room temperature. Benefiting from the large surface area, high adsorption capacity and surface hydroxyls, the alkali-promoted 3D-$NiCo_2O_4$ nanosheet catalysts show substantially high catalytic activities for HCHO oxidation. The alkali-promoted 3D-$NiCo_2O_4$ nanosheets yield a remarkable HCHO conversion efficiency of 95.3% at room temperature, which is not achieved by any non-precious metal based catalysts at such low temperature. Additionally, the as-prepared alkali-promoted 3D-$NiCo_2O_4$ nanosheets retained excellent catalytic performance after 200 h, which can be applied to practical applications. This work provides a feasible approach to improve the efficiency of metal oxides for HCHO oxidation at low temperature.

Introduction

Formaldehyde (HCHO) is one of the major volatile organic compounds in indoor air, which significantly impacts indoor air quality thus influencing human health.[1–4] Long-term exposure to HCHO will be detrimental to human health causing headache, pneumonia, and lung cancer. Among the methods employed in the removal of HCHO, catalytic oxidation had been an outstanding approach to convert HCHO into nontoxic products such as CO_2 and H_2O. Recently, noble metal-based catalysts (Pt, Au, and Pd) had been validated to display excellent catalytic performance for HCHO oxidation at room temperature.[5–9] Moreover, superb catalytic activities were achieved by surface modification with alkali.[10–12] Zhang *et al.* demonstrated that the addition of alkali-metal ions to the Pt/TiO_2 catalyst can significantly promote the performance of HCHO oxidation by enhancing the reaction between surface OH^- and formate species at room temperature.[13] Nie *et al.* found that surface hydroxyls can remarkably enhance the catalytic performance of Pt/TiO_2 toward HCHO oxidation at room temperature.[14] Avgouropoulos *et al.*[15] also reported alkali promoted Pt/Al_2O_3 catalysts for the complete oxidation of ethanol. There is a similar case that alkali obviously enhanced the catalytic performance of Ag/Co_3O_4 for HCHO oxidation due to more surface OH^- species on the catalyst surface.[16] However, due to the scarcity and expensive nature of noble metals, it is exceedingly desirable to remove HCHO at low temperature using noble-metal-free catalysts.

Recently, transition metal oxides especially those having large surface areas and high redox properties had been extensively studied as promising materials for HCHO oxidation.[17,18] Bai *et al.* reported that 3D-Co_3O_4 had much higher catalytic activity for HCHO oxidation due to its large specific surface area.[19] Additionally, as a binary metal oxide, the spinel 3D-$Mn_{0.75}Co_{2.25}O_4$ possesses much higher activity because that the coupling of two metal species could provide BMOs with rich redox reactions, which are beneficial to catalytic oxidation applications.[20] Compared with noble metal-based catalysts, the activities of transition metal oxides are not satisfactory. Therefore, it is a great challenge to develop transition metal oxide catalysts with high efficiency for HCHO oxidation at low temperature.

Spinel nickel cobaltite ($NiCo_2O_4$) has been conceived as a promising cost effective and scalable alternative since it offers many advantages such as low cost, abundant resources and environmental friendliness. In its structure, the Co^{2+} along with the Co^{3+} at the A-sites and Ni^{3+} along with the Ni^{2+} at the B-sites provide a notable catalytic activity (Scheme 1). Herein, we address novel alkali-promoted 3D-$NiCo_2O_4$ nanosheets for HCHO oxidation. Significantly, the catalyst could convert 95.3% of HCHO at a low temperature of 25 °C, which is not achieved by any non-precious metal based catalysts at such low temperature. The large surface area, high adsorption capacity and

MOE of the Key Laboratory of Bioinorganic and Synthetic Chemistry, KLGHEI of Environment and Energy Chemistry, The Key Lab of Low-carbon Chem & Energy Conservation of Guangdong Province, School of Chemistry and Chemical Engineering, Sun Yat-Sen University, 135 Xingang West Road, Guangzhou 510275, P. R. China. E-mail: jihb@mail.sysu.edu.cn; chedhx@mail.sysu.edu.cn

† Electronic supplementary information (ESI) available. See DOI: 10.1039/c5ta09370h

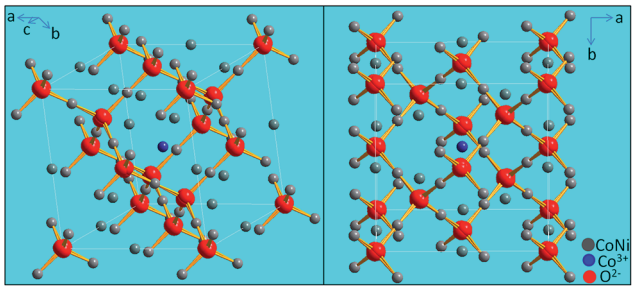

Scheme 1 Schematic unit cell structure of spinel-structured $NiCo_2O_4$.

surface hydroxyls are suggested to greatly influence the catalytic performance of alkali-promoted 3D-$NiCo_2O_4$ nanosheets. Additionally, the surface OH^- plays the main role in the reaction path of HCHO oxidation, which can directly react with formate species to produce CO_2 and H_2O.

Experimental section

Preparation of $NiCo_2O_4$ nanosheets

In a typical process, $Ni(NO_3)_2 \cdot 6H_2O$ (0.3 g), $Co(NO_3) \cdot 6H_2O$ (0.6 g), and hexamethylenetetramine (0.8 g) were dissolved in an ethanol/water solution (50 mL) with a volume ratio of 3 : 2. After being magnetically stirred for 30 min, the as-obtained homogeneous solution was transferred into a 100 mL Teflon-lined stainless steel autoclave, sealed and maintained at 95 °C for 8 h to yield a Ni–Co precursor. Subsequently, the precursor was collected by centrifugation and washed thoroughly with water and ethyl alcohol several times and dried at 60 °C for 12 h. And then the precursor was calcined in an air atmosphere at 400 °C for 3 h with 2 °C min^{-1} heating rate to obtain $NiCo_2O_4$ nanosheets. The $NiCo_2O_4$ nanosheets (0.2 g) were immersed in an aqueous solution of NaOH (KOH) (100 mL) with different concentrations (0.1, 0.5, 1, 2, and 4 M) at 80 °C. After stirring for 5 h, the catalysts were centrifuged and washed with water, and then dried at 60 °C. The resulting catalysts were denoted as $NiCo_2O_4$-0.1, $NiCo_2O_4$-0.5, $NiCo_2O_4$-1, $NiCo_2O_4$-2, and $NiCo_2O_4$-4 according to the concentration of NaOH.

Characterization

X-ray diffraction (XRD) measurements were performed using a Broker's D8 ADVANCE powder X-ray diffractometer with Cu K radiation (λ = 1.5418 Å). Transmission electron microscopy (TEM) images were obtained with a JEM2010-HR electron microscope. The morphology of the samples was investigated by using a field emission scanning electron microscope. Atomic force microscopy (AFM) images were obtained using a SPM-9500J3 microscope. X-ray photoelectron spectroscopy (XPS) measurements were performed on an ESCALab250 XPS system with an Al K_α source and a charge neutralizer, and all the binding energies were referenced to the C 1s peak at 284.8 eV of the surface adventurous carbon. Temperature-programmed reduction (TPR) analysis was conducted on a T-5080 Autochem analyzer. About 50 mg of the sample was loaded in a tube-shaped quartz cell above a small amount of quartz wool. The TPR profile of the samples was recorded between 35 °C and 600 °C at a heating rate of 10 °C min^{-1} in 10% hydrogen in N_2 with a flow rate of 50 mL min^{-1}. Hydrogen uptake was monitored by using a TCD detector. Specific surface areas (SBETs) of the catalysts were calculated from a multipoint Brunauer–Emmett–Teller (BET) analysis of the nitrogen adsorption and desorption isotherms at 77 K recorded on an Autosorb-1 apparatus. The Raman spectra were collected with a Laser Micro-Raman Spectrometer (Raman, Renishaw inVia). Fourier transform infrared spectra were recorded with a Thermo Nicolet Nexus using the KBr disk method. *In situ* diffuse reflectance infrared Fourier transformed spectra were measured on an EQVINOX-55 FFT spectroscope apparatus (Bruker) equipped with a diffuse reflectance accessory and a MCT detector. The sample was placed in a ceramic crucible in the chamber with O_2 20 vol%, about 35% relative humidity, He balance, and a total flow rate of 100 mL min^{-1}.

Thermal catalytic reaction tests

The HCHO oxidation was performed in a fixed-bed reactor with 0.2 g catalyst. HCHO gas was generated and injected into an incubator (filled with a solution of 37% HCHO) maintained at 0 °C, using a purified air flow (N_2/O_2 = 4100 mL min^{-1}). A gas hourly space velocity (GHSV) of 60 000 mL h^{-1} was applied. The products of the reaction were analyzed online by using an Agilent 7890A gas chromatograph with a TCD detector and a Porapak-Q column. No other carbon-containing compounds except CO_2 in the products were detected for all the tested catalysts. The HCHO conversion was calculated from the CO_2 content as follows:

$$\text{HCHO conversion } (\%) = [CO_2]_{out}/[HCHO]_{in} \times 100$$

$[CO_2]_{out}$ and $[HCHO]_{in}$ in the formula are the CO_2 concentration in the products and the HCHO concentration in the reactor, respectively.

Results and discussion

Synthesis and characterization of all the catalysts

3D-$NiCo_2O_4$ nanosheets were synthesized by a hydrothermal method and a post-calcination treatment (details in the Experimental section). The structural information of the samples was revealed by X-ray diffraction analysis (Fig. 1a), which verified that the final sample was spinel-structured $NiCo_2O_4$ (JCPDS 20-0781). $NiCo_2O_4$-*X* samples (*X* represents the concentration of NaOH) were obtained from the prepared $NiCo_2O_4$ by surface modification with different concentrations of alkali. Surprisingly, the phase was not changed and no residues or contaminants had been detected, revealing the high purity of the samples (Fig. 1b). The broad diffraction peaks and the intensities are weak, which indicates the low degree of crystallization and the small crystallite size of all $NiCo_2O_4$ nanosheets. In order to obtain the detailed structural information of the samples, FTIR and Raman spectroscopies were carried out. The Raman spectra show three intense peaks at about 470, 550 and 643 cm^{-1}, which are attributed to Ni–Co–O (Fig. 1c). The peaks of

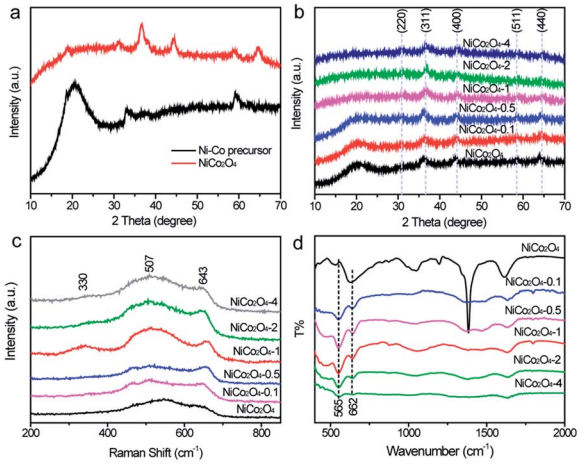

Fig. 1 (a) XRD spectra of the Ni–Co precursor and $NiCo_2O_4$. (b) XRD spectra of all the samples. (c) Raman spectra and (d) FTIR spectra of all the catalysts.

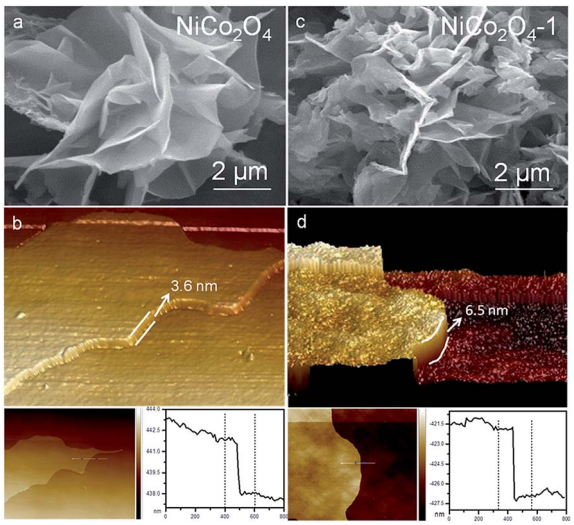

Fig. 2 (a) SEM image and (b) AFM images of $NiCo_2O_4$ nanosheets. (c) SEM image and (d) AFM images of $NiCo_2O_4$-1 nanosheets.

$NiCo_2O_4$-*X* are much stronger than those of $NiCo_2O_4$ nanosheets, which may be due to the fact that the alkali can enhance the interaction between Ni–Co–O. After NaOH treatment, the peaks were shifted. The amount of disorder in these materials, both structural and electronic, contributed to frequency shifts and band broadening. Additionally, a new peak at around 330 cm^{-1} was found for $NiCo_2O_4$-1, $NiCo_2O_4$-2, and $NiCo_2O_4$-4 samples, which has been assigned to the lattice mode involving mostly the displacement of oxygen atoms at octahedral sites.[21–23] Moreover, from FTIR spectra of catalysts, the peaks at around 662 and 565 cm^{-1} are ascribed to the metal–oxygen vibrations of the $NiCo_2O_4$ (Fig. 1d).[24,25] Furthermore, the more detailed elemental composition and the oxidation state of $NiCo_2O_4$ and $NiCo_2O_4$-*X* were further characterized by X-ray photoelectron (XPS) measurements. The surface spectra collected from the samples suggest that there are only Ni, Co, and O in the catalysts, revealing the high purity of the samples. In the Ni 2p spectrum (Fig. S1b†), the fitting peaks at 853.5 and 871 are indexed to Ni^{2+}, while those at 855.5 and 873.8 belong to Ni^{3+}. The Co 2p emission spectrum (Fig. S1c†) was fitted with spin–orbit doublets, indexed to Co^{2+} and Co^{3+}. These results show that Co^{3+}/Co^{2+} and Ni^{3+}/Ni^{2+} were present in the $NiCo_2O_4$ nanosheets, which is consistent with the results in the literature for $NiCo_2O_4$.[26,27] Battle *et al.* found that the formula of $NiCo_2O_4$ can be considered to be $Co^{(3-\delta)+}[Ni^{(2+\delta)+}Co^{3+}]O_4{}^{2-}$, which has the redox couples Co^{3+}/Co^{2+} and Ni^{3+}/Ni^{2+} and provides a notable catalytic activity.[28,29] All the aforementioned results unambiguously reveal that after surface modification with alkali the structure of $NiCo_2O_4$ is preserved.

The morphology of the catalysts was studied by scanning electron microscopy (SEM), atomic force microscopy (AFM) and transmission electron microscopy (TEM). The SEM image in Fig. 2a suggests that the $NiCo_2O_4$ possesses porous architectures that were assembled by many nanosheets. Such porous structures afford very large active surface areas, facilitating the diffusion of guest molecules. The $NiCo_2O_4$ nanosheets show a folding silk-like morphology with transparent features and the nanosheets have a thickness around 3.6 nm, indicating their ultrathin nature, as also evidenced by AFM (Fig. 2b). Surprisingly, it can be seen that the thickness of the $NiCo_2O_4$-1 nanosheets increased to 6.5 nm after the NaOH treatment. And the surface of nanosheets turns rough (Fig. 2c and d). The high resolution TEM image shows high crystallinity with an interplanar spacing of 0.468 nm, which is attributed to the *d*-spacing of the (111) planes of $NiCo_2O_4$ (Fig. 2c). The selected-area electron diffraction pattern shows well-defined diffraction rings, suggesting their polycrystalline characteristics. Significantly, an unexpected increase in thickness was found in $NiCo_2O_4$-*X* nanosheets, as displayed in Fig. 3b and S2.† In comparison with untreated $NiCo_2O_4$ nanosheets, the surface and inside of $NiCo_2O_4$-1 become disordered, which is revealed in Fig. 3d.

The results of TEM-EDS mapping of $NiCo_2O_4$-1 nanosheets reveal the homogeneous distribution of only Ni, Co, and O in the whole selection area of porous architectures, also suggesting the high purity of the samples (Fig. 3e). Moreover, the nitrogen adsorption and desorption isotherms of catalysts are shown in Fig. S3,† which belong to the IV isotherm with a hysteresis loop, indicating the presence of a porous structure

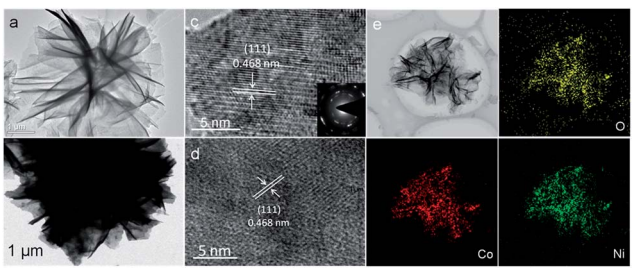

Fig. 3 TEM images of (a) untreated $NiCo_2O_4$ nanosheets and (b) $NiCo_2O_4$-1 nanosheets. HRTEM images of (c) untreated $NiCo_2O_4$ nanosheets and (d) $NiCo_2O_4$-1 nanosheets. (e) EDS elemental mapping of the same region, indicating spatial distribution of Co (red), Ni (green) and O (yellow).

in the catalysts. And the pore volume is about 0.164–0.265 $cm^3 g^{-1}$. The results of the BET analysis reveal that the surface area of untreated $NiCo_2O_4$ nanosheets (81.54 $m^2 g^{-1}$) is greater than that of $NiCo_2O_4$-*X* nanosheets (71.69–48.19 $m^2 g^{-1}$) (Table S1†).[30,31] The large surface area of $NiCo_2O_4$-*X* nanosheets may be one of the reasons why $NiCo_2O_4$-*X* nanosheets have such excellent efficiency. The higher surface area could offer more active catalytic sites for HCHO oxidation.[32]

Characterization of surface OH^- on $NiCo_2O_4$ nanosheets

To provide the fingerprint evidence for probing surface OH^-, X-ray photoelectron spectroscopy (XPS) measurements were carried out, in that the presence of surface OH^- causes distinct coordinations of oxygen species. As shown in the O 1s XPS in Fig. 4a, there is one peak at 529.5 eV in the O 1s region of $NiCo_2O_4$ nanosheets, which is attributed to the typical metal–oxygen bonds.[33] However, a new peak at 531 eV appears for the $NiCo_2O_4$-*X* nanosheets, which is associated with oxygen in OH^-. In particular, the intensity of 531 eV for $NiCo_2O_4$-1 nanosheets is much higher than that for other $NiCo_2O_4$-*X* nanosheets, indicating that the surface of the $NiCo_2O_4$ catalyst is hydroxylated to some extent as a result of surface modification with alkali. Moreover, the H_2-temperature-programmed reduction (TPR) measurements provided auxiliary evidence for the existence of surface OH^-. Fig. 4b shows the TPR spectra of the untreated $NiCo_2O_4$ and $NiCo_2O_4$-*X* catalysts. There are three peaks in the temperature range between 100 and 500 °C. They are distinguished corresponding to the consecutive stepwise reduction of Ni^{2+}, Co^{3+}, and Co^{2+} cations, statistically distributed among tetrahedral and octahedral spinel positions. Importantly, a significant enhancement in the reducibility was observed for the $NiCo_2O_4$-1 nanosheets, which have a reduction band at *ca.* 195 °C. It is reasonable to deduce that the peak at *ca.* 195 °C is due to the presence of surface OH^-, leading to enhanced catalytic activity in oxidation reactions. From the above discussion we believe that the OH^- was bonded to the surface of $NiCo_2O_4$ nanosheets rather than in the form of a crystal in the bulk. The absorption capabilities of HCHO gas were also studied to investigate the existence of surface OH^- on the $NiCo_2O_4$-*X* nanosheet catalysts (Fig. 4c). The HCHO adsorption capability over $NiCo_2O_4$ is only 9.2%, while the $NiCo_2O_4$-1 nanosheets have the largest absorption capability (15.5%) under the same conditions, indicating that the surface OH^- could obviously improve the adsorption capability toward HCHO. Combining with the XPS, TPR and absorption capability measurements above, we can conclude that surface OH^-s are successfully introduced to the $NiCo_2O_4$-*X* nanosheets and the surface OH^-s are believed to be the primary reason for the superior catalytic oxidation of HCHO.

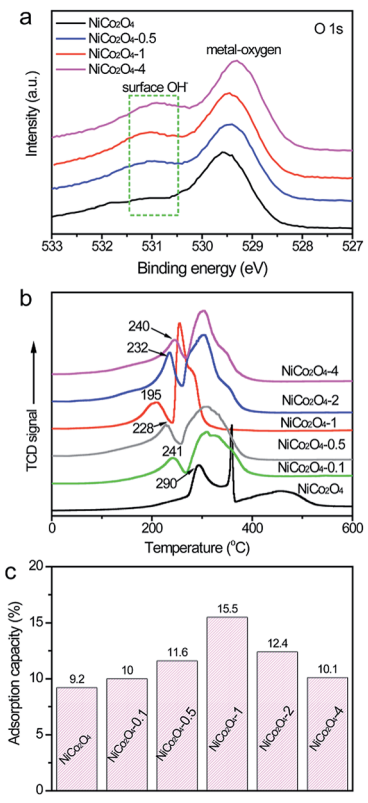

Fig. 4 (a) O 1s XPS spectra of the $NiCo_2O_4$ nanosheets, $NiCo_2O_4$-0.1 nanosheets, $NiCo_2O_4$-1 nanosheets and $NiCo_2O_4$-4 nanosheets. (b) H_2-TPR profiles and (c) adsorption capacity of all the samples.

Thermal catalytic activity of all catalysts

In order to interpret the role of surface OH^- species in catalysts, the catalytic activities of HCHO oxidation on the catalysts were evaluated. Fig. 5a shows the catalytic oxidation of HCHO as a function of temperature over different catalysts. The thermal decomposition of HCHO is negligible under our experimental conditions without catalysts. Significantly, more and more

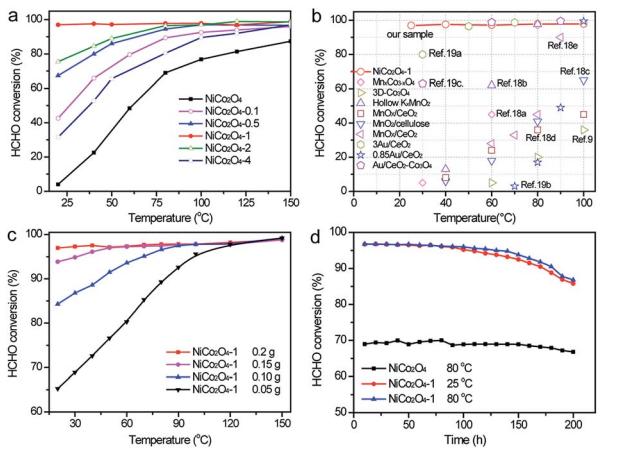

Fig. 5 (a) HCHO conversion over different catalysts as a function of temperature (HCHO concentration = 200 ppm, 25 vol% O_2, N_2 as a balance gas, the hourly space velocity GSHV = 60 000 mL h^{-1}). (b) The comparison of HCHO conversion efficiencies of our $NiCo_2O_4$-1 nanosheets with the recently reported catalysts with the same GSHV. (c) HCHO conversion over the $NiCo_2O_4$-1 nanosheet catalyst with different masses as a function of temperature. (d) Catalytic performance of HCHO over $NiCo_2O_4$-1 and $NiCo_2O_4$ nanosheets as a function of time at 25 °C and 80 °C, respectively.

HCHO is dramatically oxidized with increasing reaction temperature for all the catalysts. The untreated $NiCo_2O_4$ nanosheets could convert 79% HCHO at a temperature of 100 °C, which may be because that the $NiCo_2O_4$ nanosheets have a large specific surface area and a high redox of Co^{3+}/Co^{2+} and Ni^{3+}/Ni^{2+}. In stark contrast, all $NiCo_2O_4$-*X* nanosheet catalysts display a higher conversion efficiency than the pristine $NiCo_2O_4$ nanosheets in the entire temperature windows, indicating that surface OH^- has a positive influence on HCHO oxidation. Meanwhile, it is noteworthy that $NiCo_2O_4$-1 nanosheets exhibit a remarkably higher HCHO conversion, which could convert approximately 95% of HCHO at a low temperature of 20 °C, whereas the $NiCo_2O_4$ nanosheets only achieve 5.2% at the same temperature. It can be summarized that such excellent performance indicates that the $NiCo_2O_4$-1 nanosheets are an outstanding active thermal catalyst at the low temperature. More importantly, to the best of our knowledge, such superb efficiency is extensively lower than the values reported for any non-precious catalysts[19,34–39] and many precious catalysts.[40–42] Fig. 5b compares the HCHO conversion efficiencies of our $NiCo_2O_4$-1 nanosheets with other reported catalysts at temperatures in the range of 20 to 100 °C with the same hourly space velocity (60 000 mL h^{-1}). Additionally, the quality of catalysts is a very important factor for their conversion efficiencies. Fig. 5c displays the catalytic performance with different qualities of $NiCo_2O_4$-1 nanosheets. Without doubt, with decreasing the quality of $NiCo_2O_4$-1 nanosheets, the efficiency declines. It is noteworthy that the amount of $NiCo_2O_4$-1 nanosheets (0.05 g) could also convert 65% HCHO, further confirming the superior performance of the $NiCo_2O_4$-1 nanosheets. Moreover, superb catalytic activities are also achieved by surface modification with KOH under the same conditions, indicating that these superb catalytic activities are due to the surface OH^- (Fig. S4†). No other carbon-containing compounds except CO_2 in the products are detected for all the tested catalysts. Therefore, the above results fully indicate that the $NiCo_2O_4$-1 sample is an excellent thermal catalyst, and that surface OH^- plays an important role in the catalytic activity.

To further evaluate the stabilities of the $NiCo_2O_4$ and $NiCo_2O_4$-1 nanosheets, the catalytic performances on stream at 80 °C and 25 °C for 200 h are shown in Fig. 5d, respectively. It is worth noting that the $NiCo_2O_4$ nanosheets have ultra-high stability with only 3% decrease in the HCHO conversion efficiency after 200 h at 80 °C. In contrast, the $NiCo_2O_4$-1 nanosheets show much higher current decay over time than the $NiCo_2O_4$ catalyst. However, $NiCo_2O_4$-1 nanosheets retain 84.1% of HCHO conversion efficiency after 200 h, which indicates that $NiCo_2O_4$-1 nanosheets have excellent performance and good stability. Additionally, the morphology and phase of $NiCo_2O_4$-1 nanosheets were retained after testing for 200 h (Fig. S5†). In combination with the above experimental results, we can unambiguously conclude that the $NiCo_2O_4$-1 nanosheets have outstanding performance and good stability, which holds great significance for practical applications.

Reaction mechanism

The reaction mechanism of HCHO oxidation over $NiCo_2O_4$-1 nanosheets has been studied by the *in situ* diffuse reflectance infrared Fourier transform (DRIFTS) experiments, which have already proved to be a powerful technology for direct visualization of active species groups on the catalyst. In this regard, the *in situ* DRIFTS spectra of $NiCo_2O_4$-1 nanosheets are shown in Fig. 6. It is seen that after exposing the sample to a flow of O_2 + HCHO (37%) + He at 30 °C, the peaks appeared at 1360 and 1590 cm^{-1} belonging to the symmetric stretch and asymmetric stretch of COO; 2840 and 2950 cm^{-1} belonging to the asymmetric stretch and symmetric stretch of CH of formate, respectively. Broad peaks between 3000 and 3500 cm^{-1} can be assigned to the OH^- species on the catalyst surface. After 60 min, the intensity of the OH^- peak at 3442 cm^{-1} decreased, indicating the reaction between formate and active OH^- species on the $NiCo_2O_4$-1 nanosheet surface. It means that the pathway of the reaction for HCHO oxidation on $NiCo_2O_4$-1 nanosheets follows the HCHO → $CHOO^-$ + OH^- → CO_2 + H_2O route, which was also demonstrated in 2% Na-1% Pt/TiO_2 (ref. 13) and K–Ag/Co_3O_4.[16] Certain conclusions can be made from these studies, and the surface OH^- plays a pivotal role in proving the HCHO oxidation of $NiCo_2O_4$-1 nanosheets at low temperature, which could provide guidelines for understanding the importance of the surface OH^- for HCHO oxidation. From the above experimental results, the pronounced catalytic performance of $NiCo_2O_4$-1 nanosheets is attributed to a synergistic effect of the following factors. First, the 3D-$NiCo_2O_4$-1 nanosheets have a porous structure and a large surface area, which are good for the HCHO to diffuse and may offer more active sites for HCHO conversion. Second, more surface OH^- groups on the $NiCo_2O_4$-1 nanosheets enhanced the adsorption capacity of HCHO. Some results proposed that the adsorption over catalysts was the crucial step for HCHO oxidation, which could enable the HCHO to easily react with the catalysts. Third, the high redox of $NiCo_2O_4$-1 nanosheets enhanced the performance. The activation and migration of oxygen species on catalysts are dependent on the redox cycles of Co^{3+}/Co^{2+} and Ni^{3+}/Ni^{2+}. The increase in Co^{3+} and Ni^{2+} can enhance the redox cycles of $NiCo_2O_4$-1

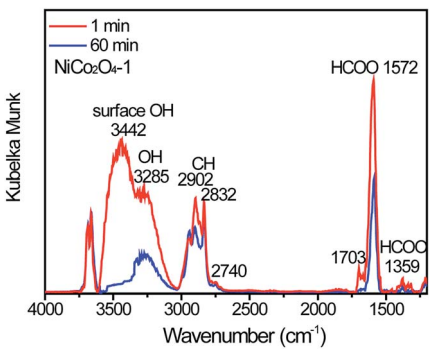

Fig. 6 *In situ* DRIFTS spectra of $NiCo_2O_4$-1 nanosheet catalysts at 30 °C at 1 min and 60 min. Reaction conditions: HCHO = 200 ppm, O_2 20 vol%, about 35% relative humidity, He balance, and a total flow rate of 100 mL min^{-1}.

nanosheets, which is favourable for the HCHO oxidation. Finally, the surface OH^- played the main role in the reaction path of HCHO oxidation, which can directly react with formate species to produce CO_2 and H_2O. Therefore, the superb catalytic performance of the $NiCo_2O_4$-1 nanosheets can be attributed to the synergistic effects of the large surface area, enhanced HCHO adsorption, the redox cycles of Co^{3+}/Co^{2+} and Ni^{3+}/Ni^{2+}, and the surface OH^-.

Conclusions

In summary, we have demonstrated novel alkali-promoted 3D-$NiCo_2O_4$ nanosheets for the HCHO oxidation. Significantly, it could convert 95.3% of HCHO into CO_2 and H_2O at a low temperature of 25 °C, which is not achieved by any non-precious metal based catalysts at such low temperature. Benefiting from the large surface area, high adsorption capacity, and high redox, the alkali-promoted 3D-$NiCo_2O_4$ nanosheet catalyst showed substantially high catalytic activity for HCHO oxidation. Additionally, the surface OH^- played the main role in the reaction path of HCHO oxidation, which can directly react with formate species to produce CO_2 and H_2O. As a consequence, the alkali-promoted 3D-$NiCo_2O_4$ nanosheets with the vital HCHO catalytic oxidation performance can be anticipated to be a candidate to replace noble metal catalysts. Furthermore, this work provides a new insight into designing low-cost and high-efficiency non-precious metal based catalysts for low-temperature thermal catalytic oxidation of VOCs.

Acknowledgements

This work was preliminarily supported by the National Science Fund for Distinguished Young Scholars (21425627), the Science and Technology Plan Project (2013B090600036), the Natural Science Foundation of China (21461162003 and 21476271), and Natural Science Foundation (2014KTSCX004 and 2014A030308012) of Guangdong Province, China.

Notes and references

1 J. Xu, T. White, P. Li, C. He and Y. F. Han, *J. Am. Chem. Soc.*, 2010, **132**, 13172–13173.
2 Q. Yuan, Z. Wu, Y. Jin, F. Xiong and W. Huang, *J. Phys. Chem. C*, 2014, **118**, 20420–20428.
3 L. Nie, J. Yu and J. Fu, *ChemCatChem*, 2014, **6**, 1983–1989.
4 Q. Wang, W. Jia, B. Liu, W. Zhao, C. Li, J. Zhang and G. Xu, *Chem.–Asian J.*, 2012, **7**, 2258–2267.
5 Z. Xu, J. Yu and M. Jaroniec, *Appl. Catal., B*, 2015, **163**, 306–312.
6 Z. Yan, Z. Xu, J. Yu and M. Jaroniec, *Environ. Sci. Technol.*, 2015, **49**, 6637–6644.
7 C. Zhang, H. He and K. i. Tanaka, *Catal. Commun.*, 2005, **6**, 211–214.
8 H. Tan, J. Wang, S. Yu and K. Zhou, *Environ. Sci. Technol.*, 2015, **49**, 8675–8682.
9 H. Huang and D. Y. Leung, *ACS Catal.*, 2011, **1**, 348–354.
10 C. Zhang, Y. Li, Y. Wang and H. He, *Environ. Sci. Technol.*, 2014, **48**, 5816–5822.
11 P. Zhou, J. Yu, L. Nie and M. Jaroniec, *J. Mater. Chem. A*, 2015, **3**, 10432–10438.
12 J. Yu, X. Li, Z. Xu and W. Xiao, *Environ. Sci. Technol.*, 2013, **47**, 9928–9933.
13 C. Zhang, F. Liu, Y. Zhai, H. Ariga, N. Yi, Y. Liu, K. Asakura, M. Flytzani-Stephanopoulos and H. He, *Angew. Chem., Int. Ed.*, 2012, **51**, 9628–9632.
14 L. Nie, J. Yu, X. Li, B. Cheng, G. Liu and M. Jaroniec, *Environ. Sci. Technol.*, 2013, **47**, 2777–2783.
15 G. Avgouropoulos, E. Oikonomopoulos, D. Kanistras and T. Ioannides, *Appl. Catal., B*, 2006, **65**, 62–69.
16 B. Bai and J. Li, *ACS Catal.*, 2014, **4**, 2753–2762.
17 Y. Huang, B. Long, M. Tang, Z. Rui, M. S. Balogun, Y. Tong and H. Ji, *Appl. Catal., B*, 2016, **181**, 779–787.
18 Z. Ren, V. Botu, S. Wang, Y. Meng, W. Song, Y. Guo, R. Ramprasad, S. L. Suib and P. X. Gao, *Angew. Chem., Int. Ed.*, 2014, **53**, 7223–7227.
19 B. Bai, H. Arandiyan and J. Li, *Appl. Catal., B*, 2013, **142**, 677–683.
20 Y. Wang, X. Zhu, M. Crocker, B. Chen and C. Shi, *Appl. Catal., B*, 2014, **160**, 542–551.
21 C. F. Windisch and G. J. Exarhos, *Vibrational Spectroscopic Study of the Site Occupancy Distribution of Cations in Nickel Cobalt Oxides*, Pacific Northwest National Laboratory (PNNL), Richland, WA (US), 2004.
22 C. F. Windisch, K. F. Ferris and G. J. Exarhos, *J. Vac. Sci. Technol., A*, 2001, **19**, 1647–1651.
23 C. F. Windisch Jr, G. J. Exarhos and S. K. Sharma, *J. Appl. Phys.*, 2002, **92**, 5572–5574.
24 P. Nkeng, G. Poillerat, J. Koenig, P. Chartier, B. Lefez, J. Lopitaux and M. Lenglet, *J. Electrochem. Soc.*, 1995, **142**, 1777–1783.
25 B. Lefez, P. Nkeng, J. Lopitaux and G. Poillerat, *Mater. Res. Bull.*, 1996, **31**, 1263–1267.
26 C. Yuan, J. Li, L. Hou, X. Zhang, L. Shen and X. W. D. Lou, *Adv. Funct. Mater.*, 2012, **22**, 4592–4597.
27 L. Shen, Q. Che, H. Li and X. Zhang, *Adv. Funct. Mater.*, 2014, **24**, 2630–2637.
28 P. D. Battle, A. K. Cheetham and J. B. Goodenough, *Mater. Res. Bull.*, 1979, **14**, 1013–1024.
29 M. Iliev, P. Silwal, B. Loukya, R. Datta, D. Kim, N. Todorov, N. Pachauri and A. Gupta, *J. Appl. Phys.*, 2013, **114**, 033514–033522.
30 Q. Wang, B. Liu, X. Wang, S. Ran, L. Wang, D. Chen and G. Shen, *J. Mater. Chem.*, 2012, **22**, 21647–21653.
31 B. Cui, H. Lin, J. B. Li, X. Li, J. Yang and J. Tao, *Adv. Funct. Mater.*, 2008, **18**, 1440–1447.
32 L. Qi, B. Cheng, J. Yu and W. Ho, *J. Hazard. Mater.*, 2015, **15**, 522–530.
33 T. Choudhury, S. Saied, J. Sullivan and A. Abbot, *J. Phys. D: Appl. Phys.*, 1989, **22**, 1185–1195.
34 C. Shi, Y. Wang, A. Zhu, B. Chen and C. Au, *Catal. Commun.*, 2012, **28**, 18–22.
35 H. Chen, J. He, C. Zhang and H. He, *J. Phys. Chem. C*, 2007, **111**, 18033–18038.

36 L. Zhou, J. He, J. Zhang, Z. He, Y. Hu, C. Zhang and H. He, *J. Phys. Chem. C*, 2011, **115**, 16873–16878.
37 J. Quiroz, J. M. Giraudon, A. Gervasini, C. Dujardin, C. Lancelot, M. Trentesaux and J. F. Lamonier, *ACS Catal.*, 2015, **5**, 2260–2269.
38 X. Tang, Y. Li, X. Huang, Y. Xu, H. Zhu, J. Wang and W. Shen, *Appl. Catal., B*, 2006, **62**, 265–273.
39 Y. Huang, H. Li, M. S. Balogun, H. Yang, Y. Tong, X. Lu and H. Ji, *RSC Adv.*, 2014, **5**, 7729–7733.
40 H. F. Li, N. Zhang, P. Chen, M. F. Luo and J. Q. Lu, *Appl. Catal., B*, 2011, **110**, 279–285.
41 Y. Shen, X. Yang, Y. Wang, Y. Zhang, H. Zhu, L. Gao and M. Jia, *Appl. Catal., B*, 2008, **79**, 142–148.
42 B. Liu, Y. Liu, C. Li, W. Hu, P. Jing, Q. Wang and J. Zhang, *Appl. Catal., B*, 2012, **127**, 47–58.